ADVANCED MATERIALS

Supporting Information

for *Adv. Mater.*, DOI 10.1002/adma.202308720

# Highly Ordered Eutectic Mesostructures via Template-Directed Solidification within Thermally Engineered Templates

*Sung Bum Kang, Guanglong Huang, Gaurav Singhal, Dajie Xie, Daniel H. Hsieh, Youngmun Lee, Ashish A. Kulkarni, John W. Smith, Qian Chen, Katsuyo Thornton*, Sanjiv Sinha and Paul V. Braun**

WILEY-VCH

# Supporting Information

## Highly Ordered Eutectic Mesostructures via Template-Directed Solidification within Thermally Engineered Templates

*Sung Bum Kang, Guanglong Huang, Gaurav Singhal, Dajie Xie, Daniel Hsieh, Youngmun Lee, Ashish A. Kulkarni, John W. Smith, Qian Chen, Katsuyo Thornton*, Sanjiv Sinha and Paul V. Braun**

Dr. S. B. Kang, G. Singhal, D. Xie, Dr. John W. Smith, Prof. Q. Chen, Prof. P. V. Braun

Department of Materials Science and Engineering, University of Illinois, Urbana, IL, 61801, USA

Materials Research Laboratory, University of Illinois, Urbana, IL, 61801, USA

E-mail: pbraun@illinois.edu

Dr. G. Huang, Prof. K. Thornton

Department of Materials Science and Engineering, University of Michigan, Ann Arbor, MI, 48109, USA

E-mail: kthorn@umich.edu

D. Hsieh, Y. Lee, Prof. S. Sinha, Prof. P. V. Braun

Department of Mechanical Science and Engineering, University of Illinois, Urbana, IL, 61801, USA

Dr. A. A. Kulkarni

Center for Functional Nanomaterials, Brookhaven National Laboratory, Upton, NY, 11973, USA

Prof. Q. Chen, Prof. P. V. Braun

Department of Chemical and Biomolecular Engineering, University of Illinois, Urbana, IL, 61801, USA

Department of Chemistry, University of Illinois, Urbana, IL, 61801, USA

Beckman Institute for Advanced Science and Technology, University of Illinois, Urbana, IL, 61801, USA

**Extracting and analysing thermal conductivity**

Experiments to measure thermal conductivity require input of heat and measurement of temperature. 3ω experiments accomplish this by heating and sensing temperature in the frequency-domain by passing current and measuring voltage from a microfabricated metal line with length much longer than width. We first describe measuring thermal conductivity of the silicon substrate. The deposited line has dimensions 1.5 mm long and 40 μm wide. The amplitude of the temperature oscillation $\Delta T$ of the metal line due to Joule heating can be obtained from the measured voltage output of the metal lines using the relationship shown by Birge and Nagel[1]:

$$\Delta T = 2V_{3\omega}\frac{R_o}{V_{1\omega}}\left(\frac{dR}{dT}\right)^{-1}, \tag{S1}$$

where $V_{3\omega}$ is the voltage amplitude at the third harmonic of the frequency of applied current, $R_o$ is the metal line electrical resistance, $V_{1\omega}$ is the voltage amplitude at the frequency of applied current ω, and $dR/dT$ is the calibrated slope of the electrical resistance with temperature. To compare the data with theory, Cahill used an approximation to the solution to the heat diffusion equation for an infinitely-thin line heat source on an infinite half-cylinder.[1] This approximation holds when the penetration depth of the thermal wave is much less than the substrate thickness and much greater than the metal line half-width. The result is

$$\Delta T_{Si} = \frac{Q}{L\pi\kappa_{Si}}\left[\frac{1}{2}\log\left(\frac{\alpha_{Si}}{b^2}\right) + \log(2) - 0.5772 - \frac{1}{2}ln\,2\omega - \frac{i\pi}{4}\right], \tag{S2}$$

where $\alpha_{Si}$ is thermal diffusivity of silicon, $L$ is the metal line length microfabricated on the Si sample, $b$ is the metal line half-width microfabricated on the Si sample. As shown in Figure 2f, on a plot of $\Delta T$ (in-phase with the heating) versus log(2ω), because the approximation holds for our sample, the data yields a straight line whose slope is inversely proportional to thermal conductivity. Therefore, we take the derivative with respect to log(2ω) of both sides of Equation (S2) to find $\kappa_{Si}$~96 W m$^{-1}$ K$^{-1}$. The magnitude is reasonable because our sample is highly doped with boron (~$10^{19}$ cm$^{-3}$) and impurity scattering reduces the thermal conductivity relative to undoped silicon (~140 W m$^{-1}$ K$^{-1}$).[2,3]

We now discuss measuring thermal conductivity of the porous silicon (pSi) film via the differential 3ω method[4]. We measure two samples that are identical except that one sample is Si and the other includes a pSi film. We determine the thermal conductivity from the difference

of the temperature oscillation between the samples, $\Delta T_{pSi-film}$, using $\Delta T_{Measured\ pSi} = \Delta T_{Si} + \Delta T_{pSi-film}$.

In our experiment, the width of the metal lines on Si are 85 μm, and on pSi 101 μm. We adjusted the current such that the heat flow to both samples was equal.

Figure 3c shows the temperature oscillation of Si and pSi samples as a function of frequency of applied current across the metal line. At frequencies 10~100 Hz, the difference in the temperature oscillation of the heater between samples is approximately constant. This is because for these frequencies the penetration depth of the thermal wave is much larger than the film thickness. This means heat flow through the film is essentially one-dimensional (1D). Therefore, we can use the Fourier law of heat conduction with the 1D resistance of a rectangular slab to model the additional temperature drop across the film, which is

$$\Delta T_{pSi-film} = \frac{Q d_{pSi}}{2bL\kappa_{pSi}}, \tag{S3}$$

where $Q$ is the amplitude of power due to Joule heating, $b$ and $L$ are as in Equation (S1) for the sample with the film, $d_{pSi}$ is the thickness of the porous Si film, and $\kappa_{pSi}$ is the thermal conductivity of the film. Combining Equations (S2)-(S3) and averaging over the frequencies where heat flows in 1D[5] yields

$$\kappa_{pSi} = d_{pSi}\left[\frac{1}{\left(\frac{2bL\Delta T}{Q}\right)_{Measured\ pSi} - \left(\frac{2bL\Delta T}{Q}\right)_{Si}}\right]_{avg\ over\ freq}. \tag{S4}$$

From this method we obtain $\kappa_{pSi}$~0.28 W m$^{-1}$ K$^{-1}$ which is much lower than the thermal conductivity of the doped silicon substrate.

**Heat transfer simulations**

Heat transfer simulations were performed using COMSOL Multiphysics® to examine the shape of the solidification front and the direction of the temperature gradient within the templates and eutectic. A schematic of the model geometry is shown in Figure S15. Heat transport within the computational domain is described by[6]

$$\rho C_p \frac{\partial T}{\partial t} - \nabla \cdot (\kappa \nabla T) = 0, \tag{S5}$$

where $\rho$, $C_p$, and κ are the density, heat capacity at constant pressure, and thermal conductivity, respectively. The COMSOL default properties for Si ($\rho_{Si} = 2.24 \times 10^3$ kg/m$^3$, $C_{p,Si} = 0.70 \times 10^3$ J/kg K, $\kappa_{Si} = 0.13 \times 10^3$ Wm$^{-1}$K$^{-1}$ and for silica glass ($\rho_{\text{glass}} = 2.20 \times 10^3$ kg/m$^3$, $C_{p,\text{glass}} = 0.70 \times 10^3$ J/(kg K), $\kappa_{\text{glass}} = 1.38$ Wm$^{-1}$K$^{-1}$) are utilized for the simulations. The density of the pure silver chloride (AgCl) and the pure potassium chloride (KCl) are $\rho_{\text{AgCl}} = 5.56 \times 10^3$ kg/m$^3$ (Solid)[7] and $\rho_{\text{KCl}} = 1.98 \times 10^3$ kg/m$^3$,[8] respectively. For simplicity, we assume that the volumes of AgCl and KCl are additive. Thus, the density of 82 wt% AgCl – 18% KCl can be estimated as follows:

$$\rho_{A\text{gCl}-\text{KCl}} = \frac{m_{\text{AgCl}-\text{KCl}}}{V_{\text{AgCl}} + V_{\text{KCl}}} = \frac{m_{\text{AgCl}-\text{KCl}}}{\frac{0.82 m_{\text{AgCl}-\text{KCl}}}{\rho_{\text{AgCl}}} + \frac{0.18 m_{\text{AgCl}-\text{KCl}}}{\rho_{\text{KCl}}}}. \quad \text{(S6)}$$

The heat capacity of pure (99.9 %) AgCl and pure (99.9 %) KCl are $C_{p,\text{AgCl}} = 0.36 \times 10^3$ J/kg K[9] and $C_{p,\text{KCl}} = 0.69 \times 10^3$ J/kg K,[10] respectively. The heat capacity of 82 wt% AgCl – 18% KCl is then estimated using rule of mixture[11]:

$$C_{p,A\text{gCl}-\text{KCl}} = 0.82 C_{p,\text{AgCl}} + 0.18\, C_{p,\text{KCl}}. \quad \text{(S7)}$$

The thermal conductivity of 82 wt% AgCl – 18% KCl was estimated to be 0.45 Wm$^{-1}$K$^{-1}$ in the literature,[12, 13] based on the thermal conductivity of the pure AgCl[9] and the pure KCl.[10] The ambient temperature is assumed to be 25 °C. The heat loss is considered to occur due to the natural air convection from the upward-facing horizontal surface of the silica glass, which is described by Newton's law of cooling. A dynamic temperature is set at the bottom boundary of the Si substrate as the boundary condition to describe the temperature change of the hot stage on which the Si substrate is placed to control the temperature of the sample. The temperature at the boundary is set to first increase from 25 °C to 400 °C at a rate of 130 °C/min and to hold at 400 °C for 5 minutes, during which the entire layer of AgCl-KCl becomes hotter than the eutectic temperature (591.73K). The boundary temperature is then continuously decreased at a rate of 2 °C/min, during which the temperature of the AgCl-KCl reduces to below the eutectic temperature. A periodic boundary condition is applied to all other boundaries.

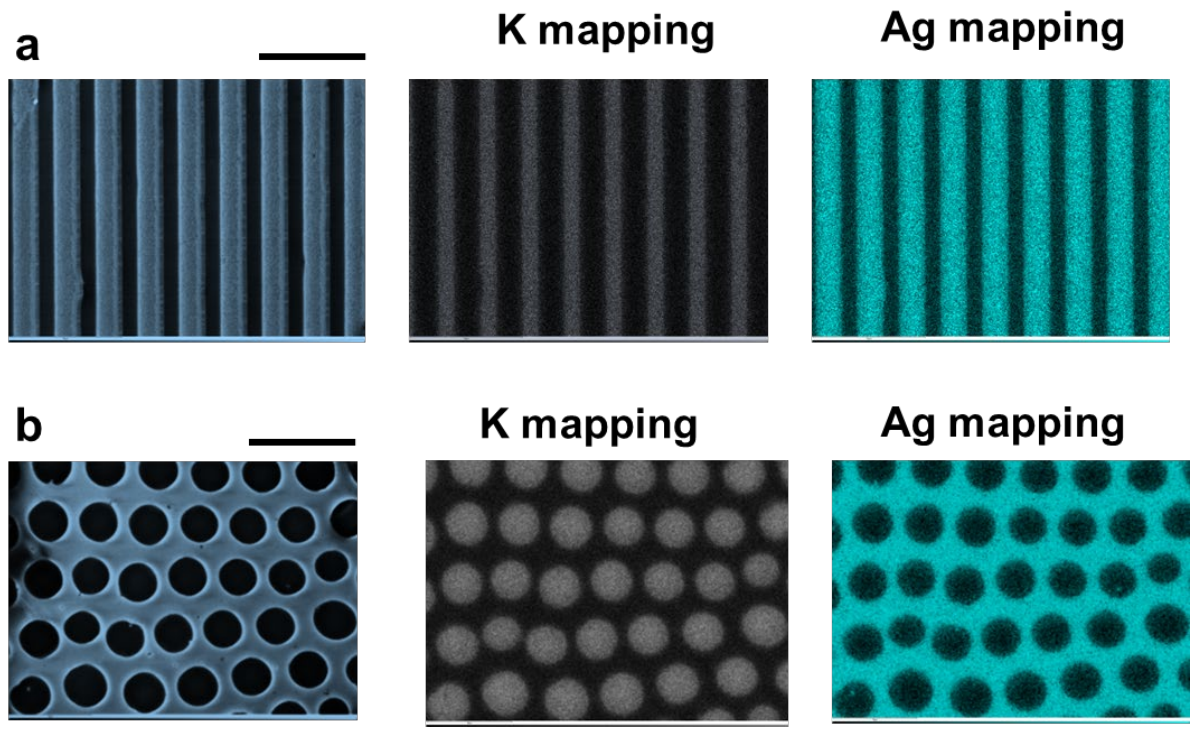



Figure S1. Top view of SEM images and EDS mapping of bulk AgCl-KCl microstructures with (a) lamellar and (b) rod patterns (scale bars: 5 μm).

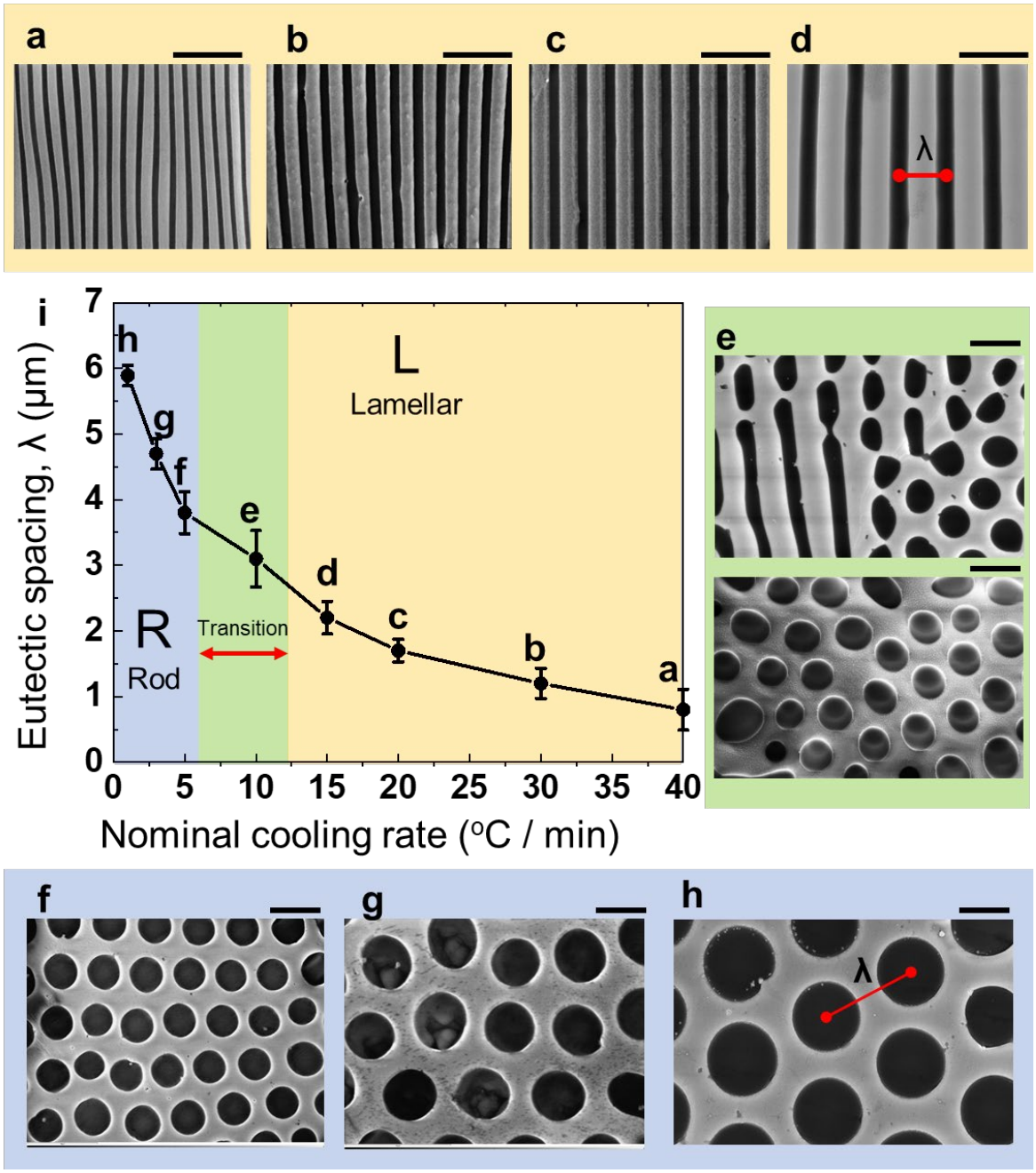



Figure S2. SEM images of microstructures formed by varying the cooling rate: (a) 40 °C / min, (b) 30 °C/min (c) 20 °C/min, (d) 15 °C/min, (e) 10 °C/min, (f) 5 °C/min, (g) 3 °C/min, and (h) 1 °C/min (scale bar: 3 μm). The eutectic lamellar/rod spacing is noted by λ. (i) Plot of eutectic spacing vs. nominal cooling rate.

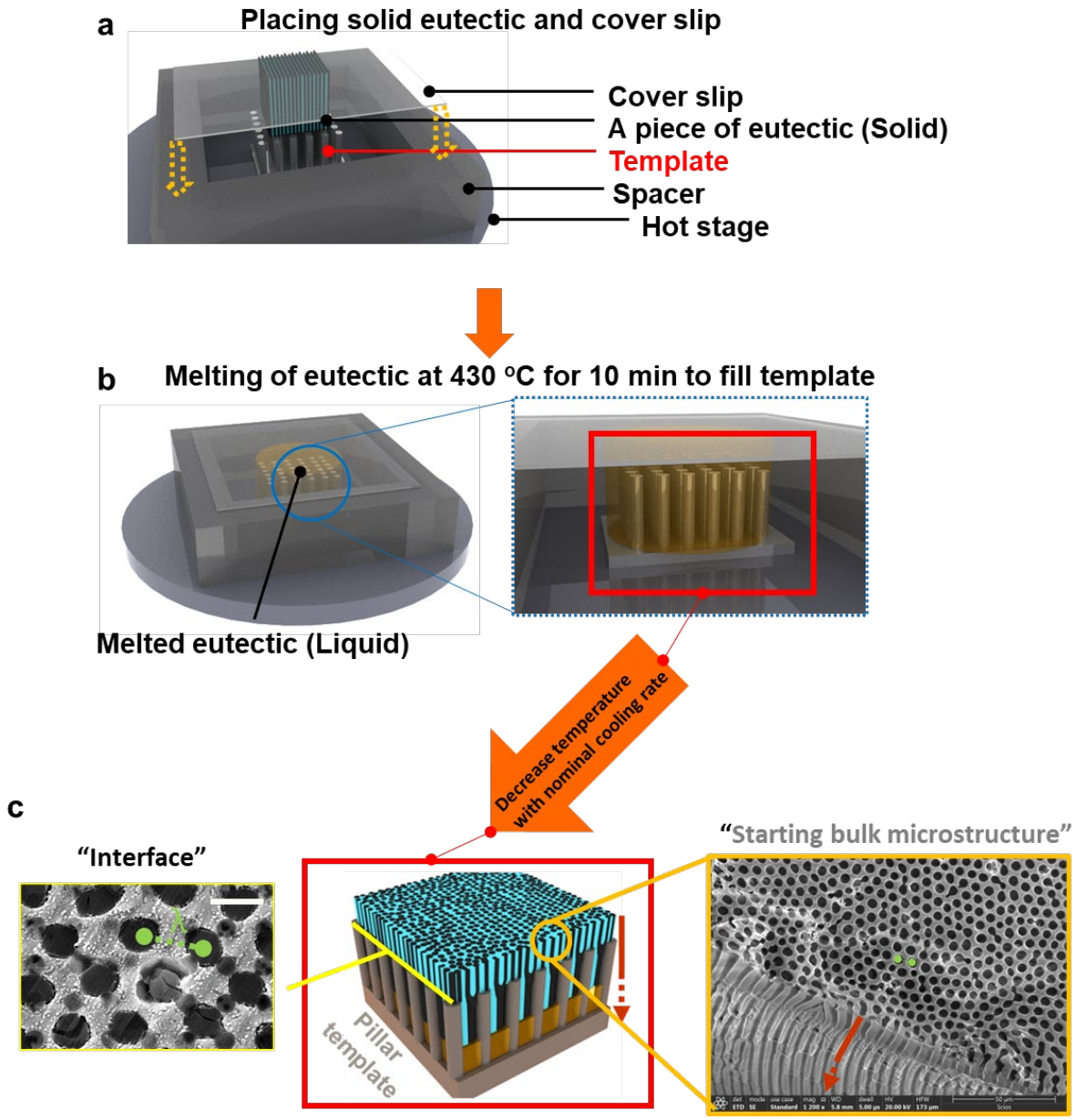



Figure S3. Setup for template-directed solidification experiment: (a) The template, positioned on a hot stage, was topped with a pre-solidified eutectic material. (b) Upon melting the pre-solidified eutectic, the resulting liquid filled the template, and the cover slip naturally descended. The liquid maintained its form as a result of the surface tension between the liquid and the glass surface. (c) The starting bulk structure is situated just beneath the cover slip, which initiates solidification as the cover slip is exposed to ambient air. The eutectic solidifies nominally at a constant rate, setting the eutectic spacing, λ. This eutectic spacing is maintained up to the very top of the template, specifically the interface between the bulk eutectic and the pillar template.

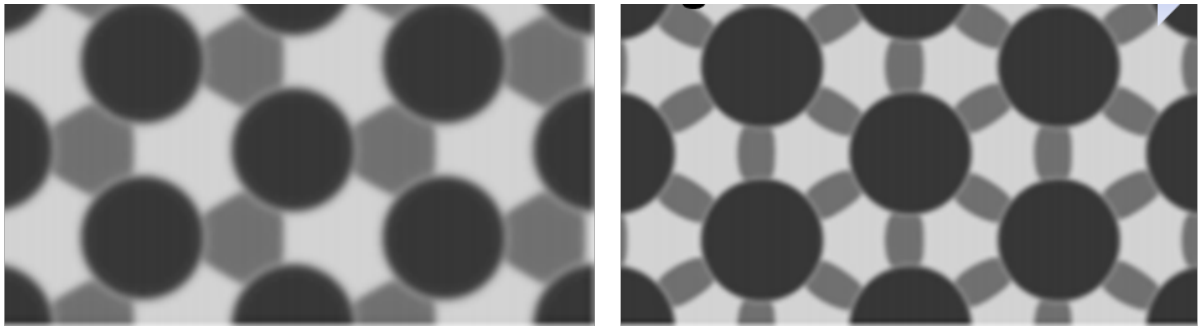


Figure S4. Phase field simulations of solidification in hexagonal array template by varying the lamellar spacing. Template volume fraction is 46 % for both panel; solidification velocities are 0.135 mm/s (left) and 0.538 mm/s (right). Simulations were conducted prior to the experiments that showed similar morphologies.

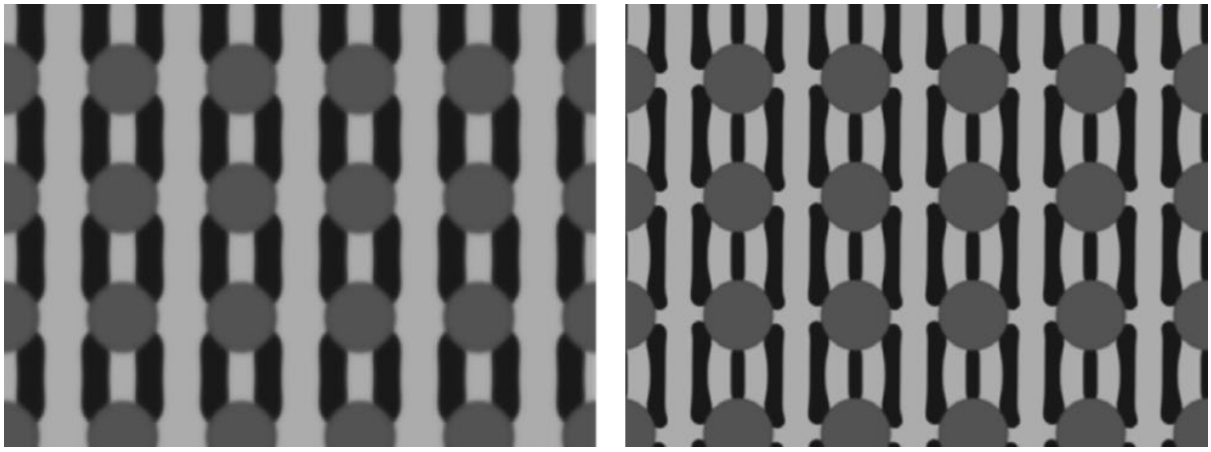


Figure S5. Phase field simulations of solidification in square array template by varying the lamellar spacing. Template volume fraction is 46 % for both panel; solidification velocities are 0.135 mm/s (left) and 0.538 mm/s (right). Simulations were conducted prior to the experiments that showed similar morphologies.

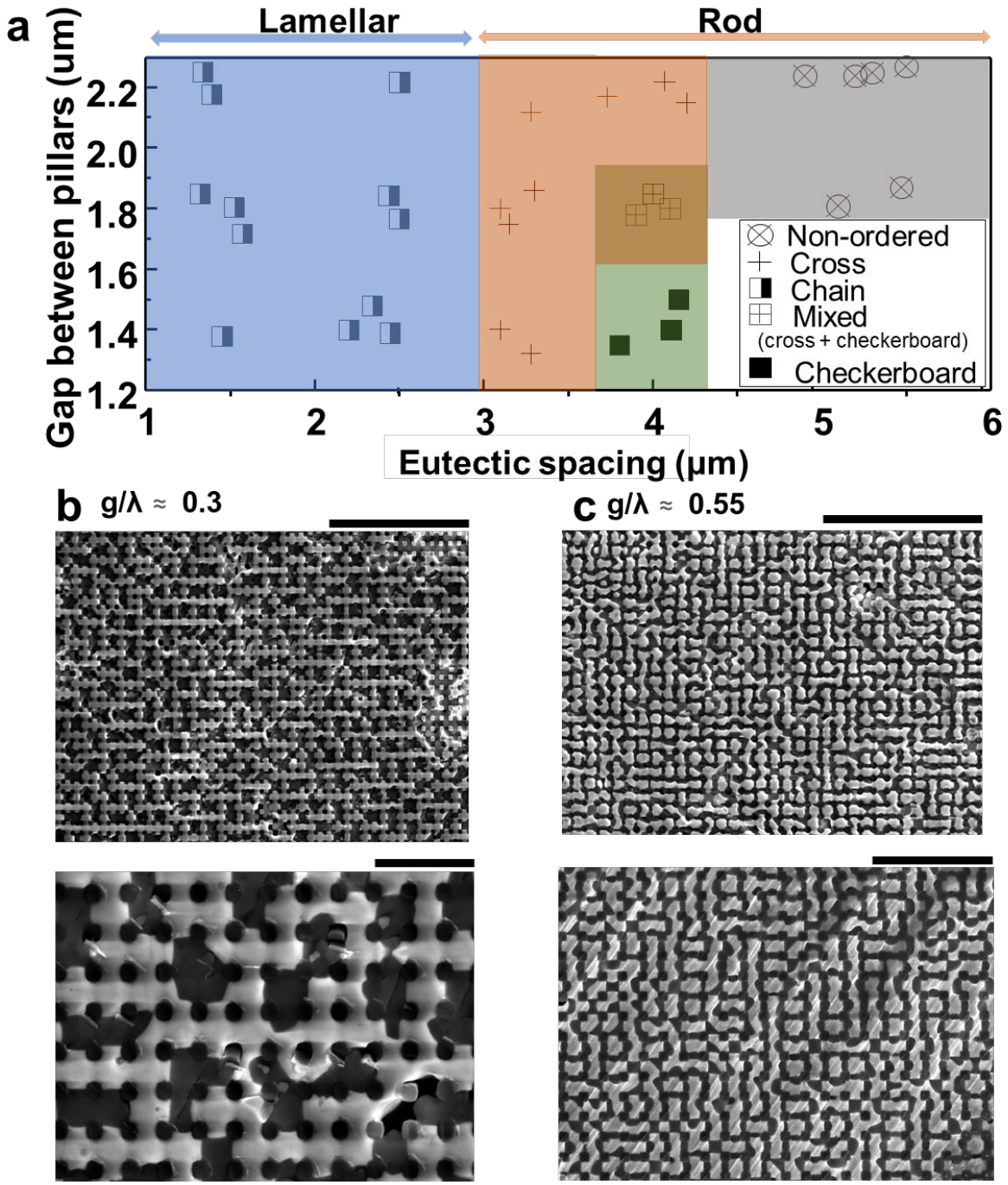



Figure S6. (a) Morphological phase map of eutectic patterns resulting from solidification in templates with square pillar lattices where pillar spacings (g) and eutectic spacings (λ) are varied. Chain (◨, blue area), checkerboard (■, green area), and cross (┼, orange area) patterns are all observed, as well as systems containing non-ordered patterns (⊗). (b) Non-ordered patterns formed from a large λ rod eutectic (λ ≈ 6 μm) solidified in a square pillar template with a pillar-to-pillar edge spacing (g) of 1.8 μm (scale bar: 50 μm (top) and 10 μm (bottom)). (c) Randomly distributed two-spoke and four-spoke patterns formed by a small λ rod eutectic (λ ≈ 3.5 μm) solidified in a square pillar template with a pillar-to-pillar edge spacing (g) of 1.8 μm (scale bar: 50 μm (top) and 20 μm (bottom)). The template is made of Si.

**Morphological phase diagram and description of patterns emerging from template-directed eutectic solidification**

The correlation between self-assembled patterns, the distance between pillars in the template, and eutectic spacing is depicted in a morphological phase diagram (Figure S6a). When a bulk AgCl-KCl lamellar eutectic is solidified into a hexagonal template, Archimedean lattices emerge (e.g., Figure 1b&c), and when solidified in a square template, chain patterns emerge (e.g., Figure 1d&e). When a bulk AgCl-KCl rod eutectic is solidified in the square or rectangular templates, patterns including four-spoked crosses and checkerboard configurations result (e.g., Figure 1f-i). We note the patterns of Fig. 1f-i all contain elements of the native eutectic rod structure, with KCl existing in essentially a rod configuration.[14] A non-ordered pattern results when a rod eutectic with characteristic dimensions considerably larger than the template (like the eutectic of Figure S2h) is solidified in the template (Figure S6b, $g/\lambda \approx 0.3$). By modifying the pillar template's geometry to a rectangular grid or by altering the pillar's shape while maintaining the same $g/\lambda$, patterns such as elongated checkerboards or inverse cross patterns (Figure 1h and i) can result. It is noted that rod structures with small rod spacing are on the cusp of changing to a lamellar structure (Figure S2e), and, at this solidification rate, the structure within the template is a mixed chain and cross pattern configuration (Figure S6c, $g/\lambda \approx 0.55$).

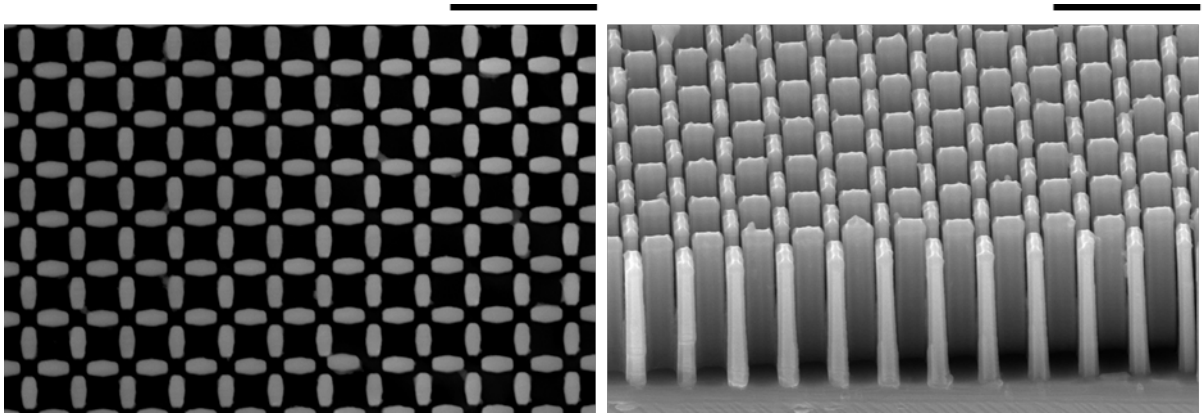


Figure S7. Si rectangular pillar square array template (scale bar: 10 μm for both images).

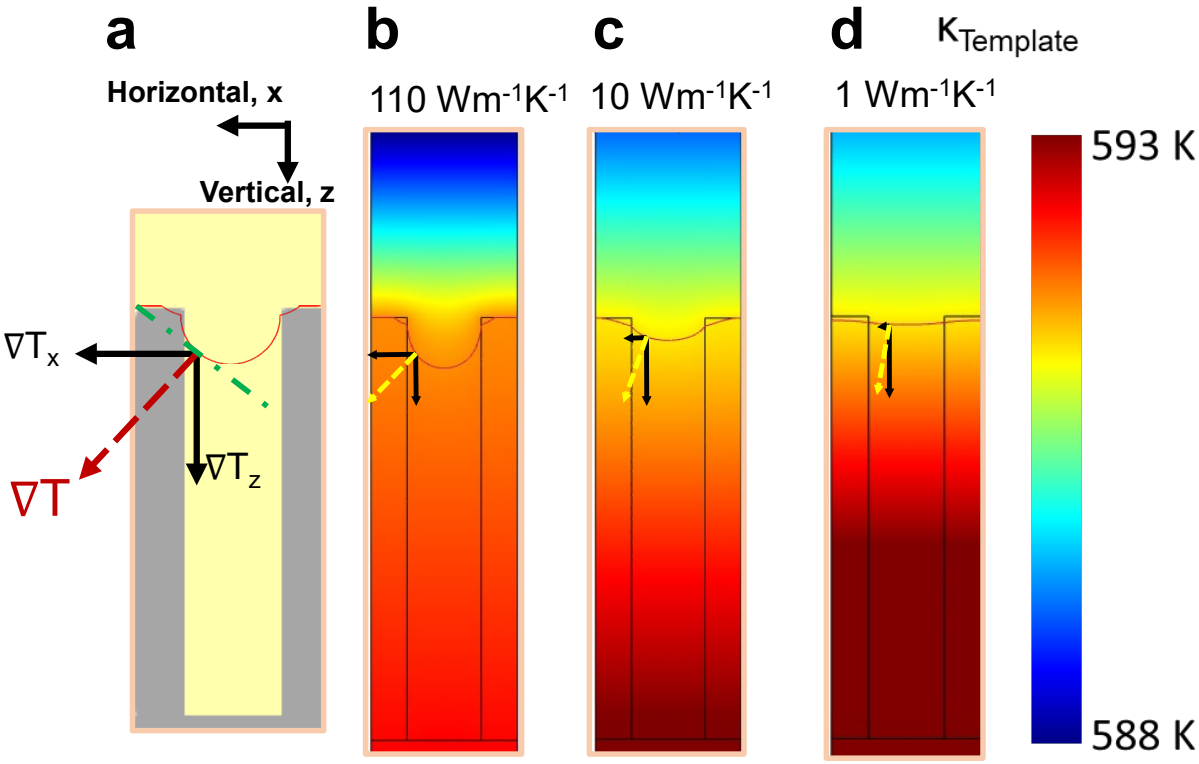



Figure S8. (a) The temperature gradient is schematically shown as the perpendicular vector of a tangent line (green line) drawn on the isothermal line in the indicated plane. (b-d) The 2D cross-sectional view of the temperature profile and the isothermal surface at eutectic temperature when using templates with thermal conductivity values of: (b) 110 W $m^{-1}K^{-1}$, (c) 10 W $m^{-1}K^{-1}$, and (d) 1 W $m^{-1}K^{-1}$, taken when t = 2438.9s. The cross section is obtained at one of the computational domain boundaries (specifically, y=0, but all four faces are equivalent due to the symmetry).

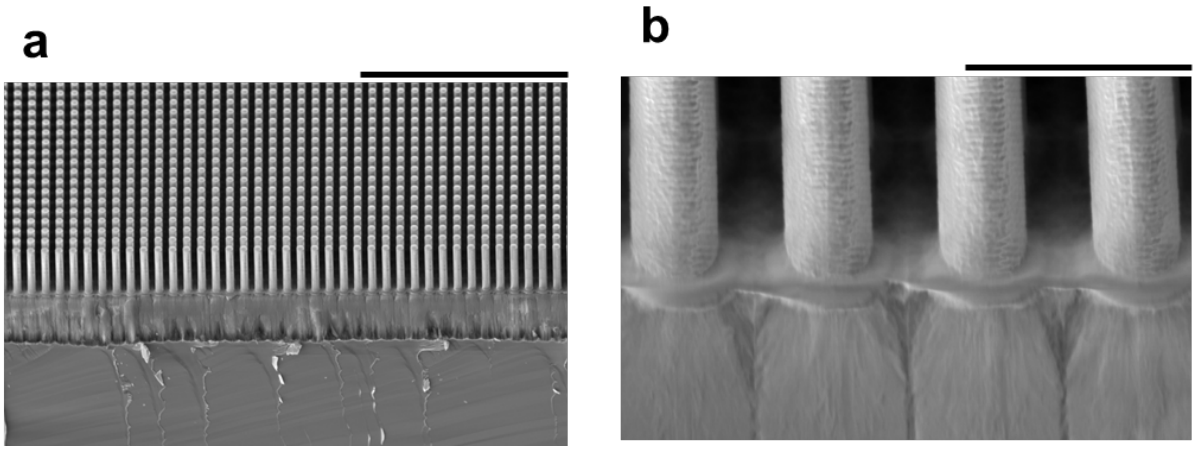



Figure S9. SEM images of thermally engineered template based on porosifed Si pillar arrays: (a) tilted view (scale bar: 50 μm) and (b) bottom region of porosified Si pillars (scale bar: 5 μm).

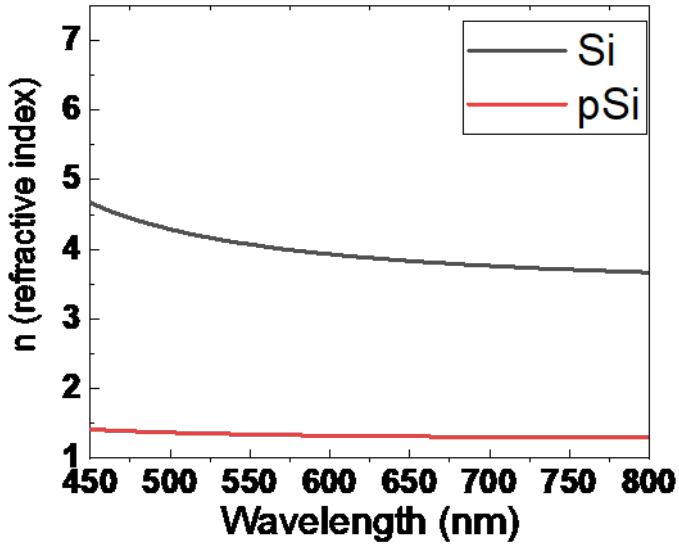



Figure S10. Refractive index of Si and PSi as function of wavelength. The porosity of pSi is estimated by using the Bruggeman effective medium theory.[15] The refractive index of Si is 3.87 and the measured refractive index of pSi is 1.3174 at 630nm. The pSi porosity is calculated to be 81%. The porosity is given by the solution to

$$p\left(\frac{1-n_{pSi}^2}{1+2n_{pSi}^2}\right)+(1-p)\left(\frac{n_{Si}^2-n_{pSi}^2}{n_{Si}^2+2n_{pSi}^2}\right)=0,$$

where $p$ is porosity, $n_{pSi}$ is refractive index of pSi, and $n_{Si}$ is refractive index of Si.

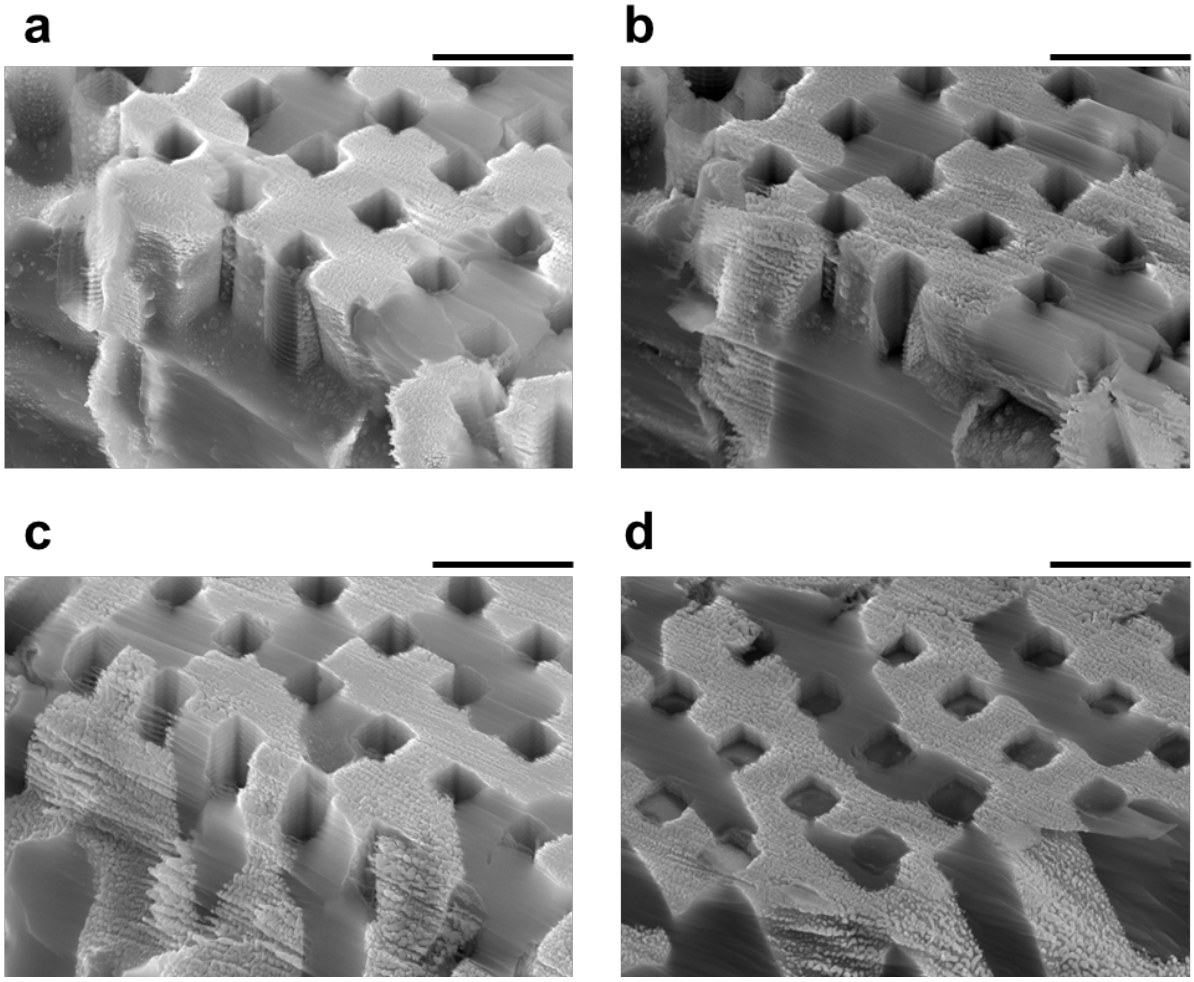



Figure S11. SEM images of the pattern after each etch step: (a) before etching, (b) after etching of 2.5 µm, (c) after etching of 5 µm and (c) after etching of 7.5 µm from the top (scale bar: 5 µm).

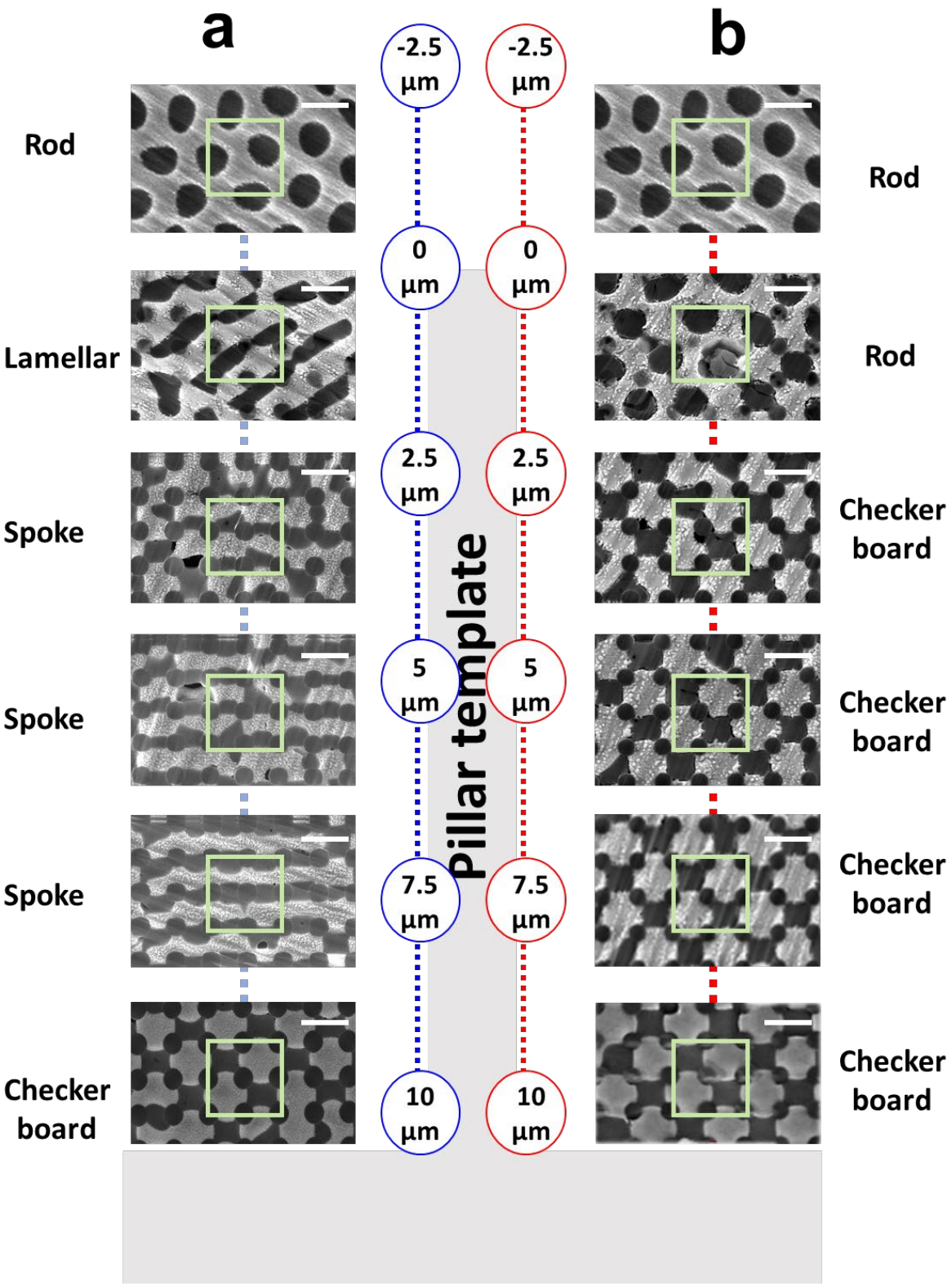



Figure S12. SEM images of pattern from solidification in (a) Si pillar template (with high thermal conductivity) and (b) pSi pillar template (with low thermal conductivity). Green box indicates template symmetry. 0 µm is the top of the pillars and 10 µm is the bottom of the pillars.

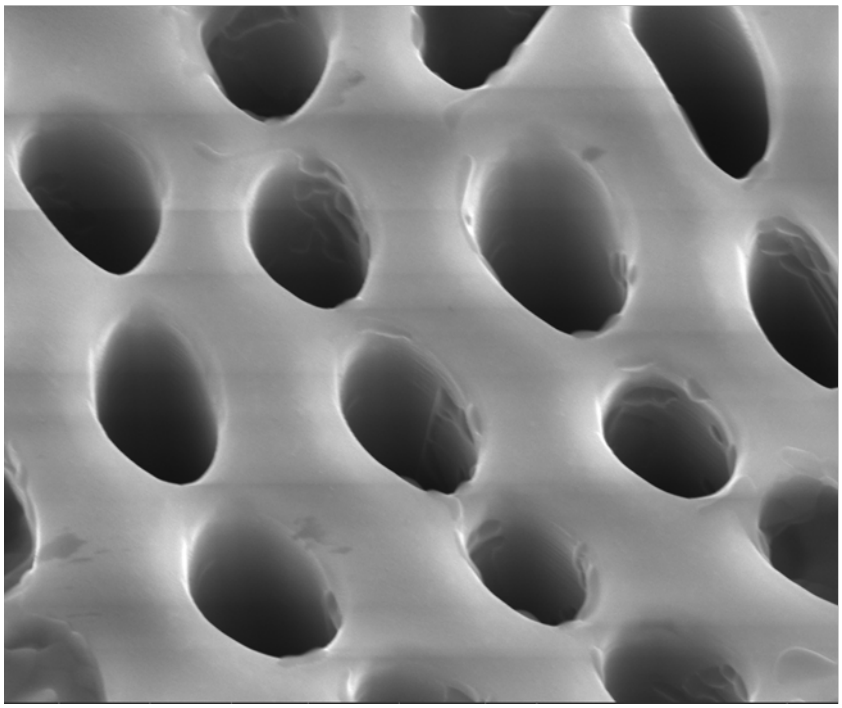


Figure S13. SEM image of bulk rod eutectic structure after etching of KCl by water (scale bar: 5 μm).

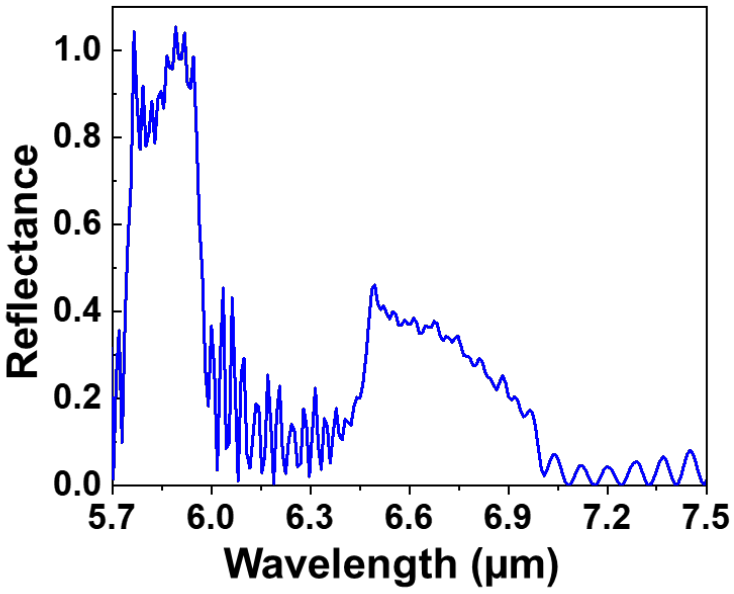



Figure S14. Simulated reflectance spectrum of checkerboard pattern after removal of KCl and porous Si pillar array.

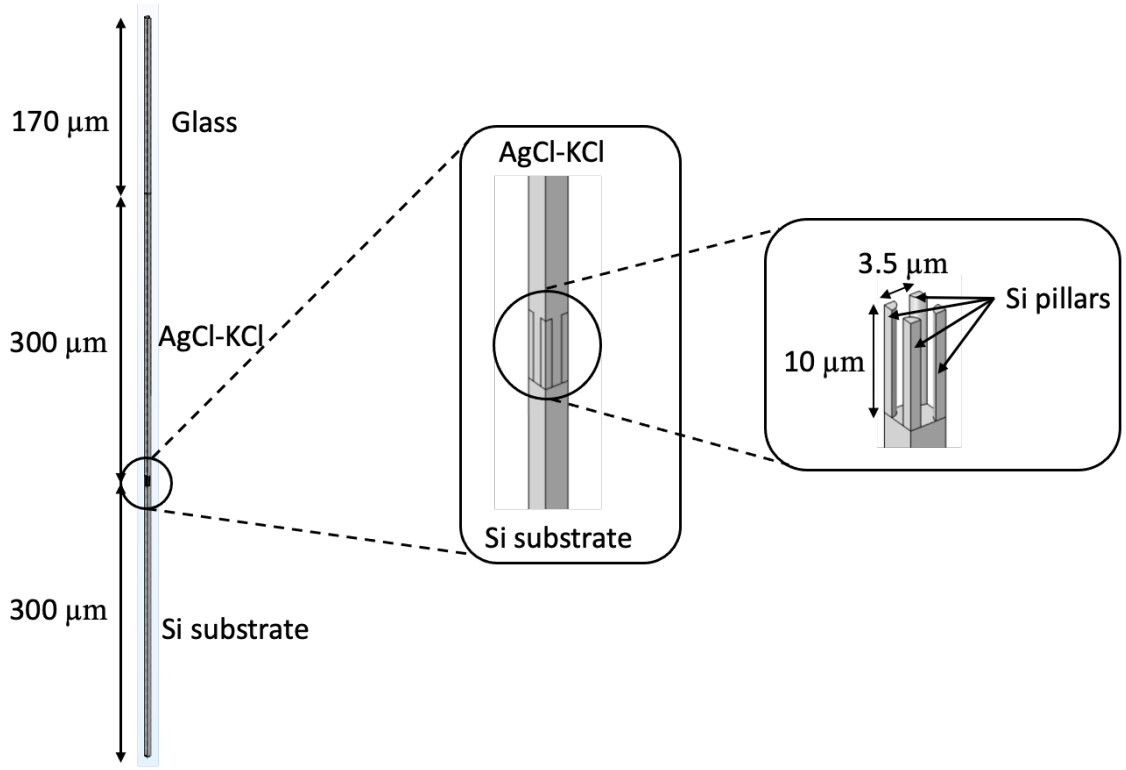



Figure S15. Schematic of the heat transfer model geometry.

**References**

[1] Cahill, D. G. (1990). Thermal conductivity measurement from 30 to 750 K: The 3ω method. *Review of Scientific Instruments*, 61(2), 802–808. https://doi.org/10.1063/1.1141498

[2] Asheghi, M., Kurabayashi, K., Kasnavi, R., & Goodson, K. E. (2002). Thermal conduction in doped single-crystal silicon films. *Journal of Applied Physics*, 91(8), 5079-5088. https://doi.org/10.1063/1.1458057

[3] Slack, G. A. (1964). Thermal conductivity of pure and impure silicon, silicon carbide, and diamond. *Journal of Applied Physics*, 35(12), 3460-3466. https://doi.org/10.1063/1.1713251

[4] Cahill, D. G., Katiyar, M., & Abelson, J. R. (1994). Thermal conductivity of a -Si:H thin films. *Physical Review B*, 50(9), 6077–6081. https://doi.org/10.1103/PhysRevB.50.6077

[5] Borca-Tasciuc, T., Kumar, A. R., & Chen, G. (2001). Data reduction in 3ω method for thin-film thermal conductivity determination. *Review of Scientific Instruments*, 72(4), 2139-2147. https://doi.org/10.1063/1.1353189

[6] F. P. Incropera, D. P. DeWitt, T. L. Bergman and A. S. Lavine, Fundamentals of heat and mass transfer, John Wiley & Sons, 6th edn., 2007.

[7] R. C. Weast, Handbook of Chemistry and Physics, Springer, 1988.

[8] D. A. Hutchison, Density of potassium chloride. *Phys Rev*, 1944, 66, 144-148.

[9] CRYSTRAN, Silver chloride (AgCl) data sheet, https://www.crystran.co.uk/optical-materials/silver-chloride-agcl, (accessed February 3 2023).

[10] CRYSTRAN, Potassium Chloride (KCl) Data Sheet, https://www.crystran.co.uk/optical-materials/potassium-chloride-kcl, (accessed February 3 2023).

[11] D. Günther and F. Steimle, Mixing rules for the specific heat capacities of several HFC-mixtures. *International Journal of Refrigeration*, 1997, 20, 235-243.

[12] J. W. Boley, K. Chaudhary, T. J. Ober, M. Khorasaninejad, W. T. Chen, E. Hanson, A. Kulkarni, J. Oh, J. Kim, L. K. Aagesen, A. Y. Zhu, F. Capasso, K. Thornton, P. V. Braun and J. A. Lewis, High-operating-temperature direct ink writing of mesoscale eutectic architectures. *Advanced Materials*, 2017, 29, 1604778.

[13] A. A. Kulkarni, E. Hanson, R. Zhang, K. Thornton and P. V. Braun, Archimedean lattices emerge in template-directed eutectic solidification. *Nature*, 2020, 577, 355-358.

[14] S. Liu, J.H. Lee, R. Trivedi, Dynamic effects in the lamellar–rod eutectic transition, *Acta Materialia,* 2011, 59, 3102-3115*,*

[15] S. Bosch, J. Ferre-Borrull, N. Leinfellner, A. Canillas, Effective dielectric function of mixtures of three or more materials: a numerical procedure for computations. *Surface Science*, 2000, 453, 9.